PNAS RESEARCH ARTICLE | BIOPHYSICS AND COMPUTATIONAL BIOLOGY

Phase separation of intrinsically disordered FG-Nups is driven by highly dynamic FG motifs

Maurice Dekker[a], Erik Van der Giessen[a], and Patrick R. Onck[a,1]

Edited by J. McCammon, University of California San Diego, La Jolla, CA; received December 23, 2022; accepted May 9, 2023

The intrinsically disordered FG-Nups in the central channel of the nuclear pore complex (NPC) form a selective permeability barrier, allowing small molecules to traverse by passive diffusion, while large molecules can only translocate with the help of nuclear transport receptors. The exact phase state of the permeability barrier remains elusive. In vitro experiments have shown that some FG-Nups can undergo phase separation into condensates that display NPC-like permeability barrier properties. Here, we use molecular dynamics simulations at amino acid resolution to study the phase separation characteristics of each of the disordered FG-Nups of the yeast NPC. We find that GLFG-Nups undergo phase separation and reveal that the FG motifs act as highly dynamic hydrophobic stickers that are essential for the formation of FG-Nup condensates featuring droplet-spanning percolated networks. Additionally, we study phase separation in an FG-Nup mixture that resembles the NPC stoichiometry and observe that an NPC condensate is formed containing multiple GLFG-Nups. We find that the phase separation of this NPC condensate is also driven by FG–FG interactions, similar to the homotypic FG-Nup condensates. Based on the observed phase separation behavior, the different FG-Nups of the yeast NPC can be divided into two classes: The FG-Nups (mostly GLFG-type) located in the central channel of the NPC form a highly dynamic percolated network formed by many short-lived FG–FG interactions, while the peripheral FG-Nups (mostly FxFG-type) at the entry and exit of the NPC channel likely form an entropic brush.

FG-Nups | phase separation | nuclear pore complex | intrinsically disordered proteins

Significance

The selective permeability barrier of the nuclear pore complex (NPC) is crucial for the homeostatic functioning of eukaryotic cells. The phase state of this barrier, composed of multiple intrinsically disordered phenylalanine–glycine (FG) repeat proteins, is not known and under intense debate. Here, we show that more than half of the FG-Nups form liquid-like condensates and that the FG motifs are essential in doing so, forming highly dynamic hydrophobic FG–FG cross-links with interaction life times below 1 ns. Furthermore, our findings suggest that the FG-Nups of the NPC can be categorized into two classes: GLFG-Nups that phase separate and FxFG-Nups that do not, suggesting distinct roles in establishing the NPC's permeability barrier.

Nuclear pore complexes (NPCs) are the sole gateways for molecules to transit between the cytoplasm and the nucleus. NPCs are large protein complexes that have a highly selective permeability barrier, allowing small molecules to pass through by passive diffusion, while the transport of larger molecules is significantly reduced, unless they are bound to nuclear transport receptors (NTRs). The central channel of the NPC is lined with intrinsically disordered nucleoporin proteins containing many phenylalanine/glycine (FG) motifs, i.e., FG-Nucleoporins (FG-Nups). These FG motifs have been shown to play an essential role in NTR-driven transport (1, 2) and are also suggested to be important in maintaining the passive permeability barrier of the NPC (3–5). Various descriptions exist that relate the phase state of the FG-Nups in the NPC central channel to its selectivity: The selective phase model (6, 7) proposes that the FG-Nups form a dense, sieve-like meshwork through specific FG–FG interactions that allows small particles to pass, while blocking larger molecules. In the virtual gate model (8, 9), the NPC selectivity is ascribed to an entropic barrier formed by the FG-Nups: small particles have a small entropic penalty and can easily cross the NPC, while the big entropic penalty for large particles makes them less likely to traverse the NPC. The forest model (10) relates Nup-associated transport to the bimodal distribution of charges along the FG-Nups sequences, giving rise to molecules with an extended and a collapsed domain. This bimodal conformational character is proposed to lead to a variation of FG-Nup densities inside the NPC, resulting in different transport pathways for passive and NTR-driven transport. Finally, the Kap-centric model (11, 12) is based on the premise that NTRs are an integral part of the NPC and thus must play an important role in its barrier and transport function.

In recent years, phase separation has been recognized to be a powerful mechanism of cells to organize their cytoplasm and nucleoplasm and to catalyze molecular interactions through the formation of locally high concentrations of interacting molecules (13, 14). Being omnipresent in cells and vital for a wide range of biological processes (15), phase separation has gained much attention, with a specific focus on RNA binding proteins (RBPs) and RNA-transcription (16–20). Many RBPs contain low-complexity domains that are intrinsically disordered and can phase separate into liquid-like condensates.

Author affiliations: [a]Zernike Institute for Advanced Materials, University of Groningen, 9747 AG, Groningen, The Netherlands

Author contributions: M.D., E.V.d.G., and P.R.O. designed research; M.D. performed research; M.D. contributed new reagents/analytic tools; M.D. analyzed data; and M.D., E.V.d.G., and P.R.O. wrote the paper.

The authors declare no competing interest.

This article is a PNAS Direct Submission.

[1]To whom correspondence may be addressed. Email: p.r.onck@rug.nl.

This article contains supporting information online at https://www.pnas.org/lookup/suppl/doi:10.1073/pnas.2221804120/-/DCSupplemental.

Published June 12, 2023.

The main physicochemical drivers of this process have been identified to be cation–π interactions (21–24).

Experiments have shown that FG-Nups can also undergo phase separation into liquid condensates (25), hydrogels (3, 7, 26–30), and even amyloid-like structures (31–35). Most experiments focus on the formation of FG-Nup hydrogels, which show similar permeability properties as the NPC barrier (3, 7, 26). Interestingly, recent work has shown that in the first stage of phase separation, the FG-Nup condensates display typical properties of a liquid state and that this liquid-like state is already enough to mimic the selectivity of the NPC permeability barrier (25). These in vitro results, together with the important role of FG-Nup condensation in NPC biogenesis in vivo (36), point to phase separation of FG-Nups as a possible organizing principle utilized by the cell in facilitating NPC assembly and selective transport.

FG-Nup sequences exhibit a relatively low complexity with FG motifs being interspaced by mostly polar amino acids. Due to the low abundance of charged residues in FG-Nups, electrostatic and cation–π interactions are not expected to play a dominant role, suggesting that phase separation of FG-Nups is driven by different molecular interactions than in the well-characterized RBP low-complexity domains.

Experimental studies of the propensity for phase separation of FG-Nups have demonstrated phase transitions for Nup116 (28, 34), Nup100 (28, 34), Nup145N (34), Nup49 (25), and Nsp1 (7, 26, 31, 37). In addition, Patel et al. (38) have used bead-immobilized FG-Nups at high concentrations mixed with soluble fluorescently labeled FG-Nups to characterize the low-affinity protein interactions of all FG-Nups in yeast. Their experiments demonstrate the presence of homotypic attractive interactions for the FG domains of Nup116, Nup100, Nup145N, Nup49, Nup57, and Nup42 both in vivo and in vitro and the absence of such low-affinity interactions for Nup159, Nsp1, Nup1, Nup2, and Nup60. Although these bead assays give valuable insights, a complete phase separation assessment evaluating the phase separation characteristics for all yeast FG-Nups and their different domains is missing. Here, we investigate phase separation of FG-Nups by carrying out coarse-grained molecular dynamics (CGMD) simulations using a one-bead-per-amino-acid (1BPA) MD model (39–41). This model has been used previously to study nuclear transport through the yeast NPC (40, 42–47) and biomimetic nanopores (48–52) and to analyze the phase separation of dipeptide repeat proteins (53). In the present paper, we show that several intrinsically disordered FG-Nups of the yeast NPC undergo phase separation coupled to percolation. We find that the FG-Nup condensates involve droplet-spanning percolated networks stabilized by highly dynamic interactions between the hydrophobic FG motifs that line the FG-Nup sequences. Additionally, we study phase separation of an FG-Nup mixture that resembles the exact NPC stoichiometry and observe the formation of a highly dynamic condensate containing multiple types of GLFG-Nups. From intermolecular contact statistics of the different types of FG-Nups, we find that the phase separation of this NPC condensate is also driven by FG–FG interactions, similar to the homotypic FG-Nup condensates. Based on these findings, the intrinsically disordered FG-Nups of the yeast NPC can be divided into two groups: GLFG-Nups that show phase separation coupled to percolation and FxFG-Nups that do not phase separate. By relating the phase separation behavior to their anchor location inside the NPC, our results point to different functional roles for the two groups in mediating nuclear transport.

Results

Selection of FG Domains. This study is confined to those FG-Nup domains in the yeast NPC that contain FG motifs and lack any ordered secondary structures (Fig. 1). To identify these domains, we first determined the disordered domain for each FG-Nup using three different disorder predictors to minimize the effect of bias and over/underprediction of disorder (54). The disorder prediction scores show significant differences but generally agree well on the location of the boundary between ordered and disordered domains. Kim et al. (55) also identified the disordered domains for each of the FG-Nups that constitute the yeast NPC. These domains are highlighted in Fig. 1, where we considered both the intrinsically disordered and the flexible linker domains as part of the disordered domain. This choice is supported by the excellent agreement with the disorder prediction scores of the linkers. Nup2 (not present in the data of Kim et al.) has an ordered domain at its C terminal (AA 601–708) (56), in good agreement with the disorder prediction scores.

Having identified the disordered domains of the FG-Nups, we selected the FG domains that contain all FG motifs from the disordered domain (see Fig. 1, blue domains). Unless stated otherwise, these are the domains that are used in our simulations.

Phase Separation of FG-Nups Is Driven by FG Motifs. To study the phase separation characteristics of FG-Nups, we evaluate the phase separation behavior of the FG domain of all FG-Nups (indicated in blue in Fig. 1) using 1BPA molecular dynamics simulations. To speed up the equilibration process, all simulations are initiated from a high-density protein condensate structure (see Fig. 2, starting configuration). Within 2 μs of simulation time, all systems have reached a dynamic equilibrium state (*SI Appendix*, Fig. S3), which is either a stable liquid-like condensate surrounded by a low concentration of free monomers in the case of phase separation or a homogeneous monomer solution when there is no phase separation. See *Materials and Methods* for more details.

Stable FG-Nup condensates are found for Nup116, Nup100, Nup145N, Nup49, Nup57, and Nup42 (Fig. 2). Each of these condensates is in dynamic equilibrium with the surrounding solvent, meaning that the rate at which molecules leave the condensate is equal to the rate at which molecules enter the condensate (*SI Appendix*, Fig. S3). Using radial density distributions, we have determined the concentrations of the dense phase and the dilute phase for each of the FG-Nup condensates (*SI Appendix*, Fig. S4). The density of the condensates is comparable for each of the GLFG-Nups (ρ_H = 350 to 400 mg/mL) and is in good agreement with in vitro experiments (25, 28, 60). Surprisingly, the dense concentration for condensates with practically no dilute phase (i.e., Nup100 and Nup116) is slightly lower than for some condensates where a dilute phase is present (i.e., Nup57 and Nup145N). This suggests that there is no relation between the concentration of the dense phase, ρ_H, and the concentration of the dilute phase, ρ_L. On the other hand, we do observe that the concentration of the dilute phase is significantly higher for the shorter FG-Nups (i.e., Nup49, Nup57, and Nup145N), suggesting that the FG-Nup length also plays an important role in the phase separation behavior, as was previously observed for dipeptide repeat proteins (53). To investigate this further, we have performed an additional phase separation simulation where we attached two FG domains of Nup49 together (referred to as Nup49x2). We find that Nup49x2 phase separates as well

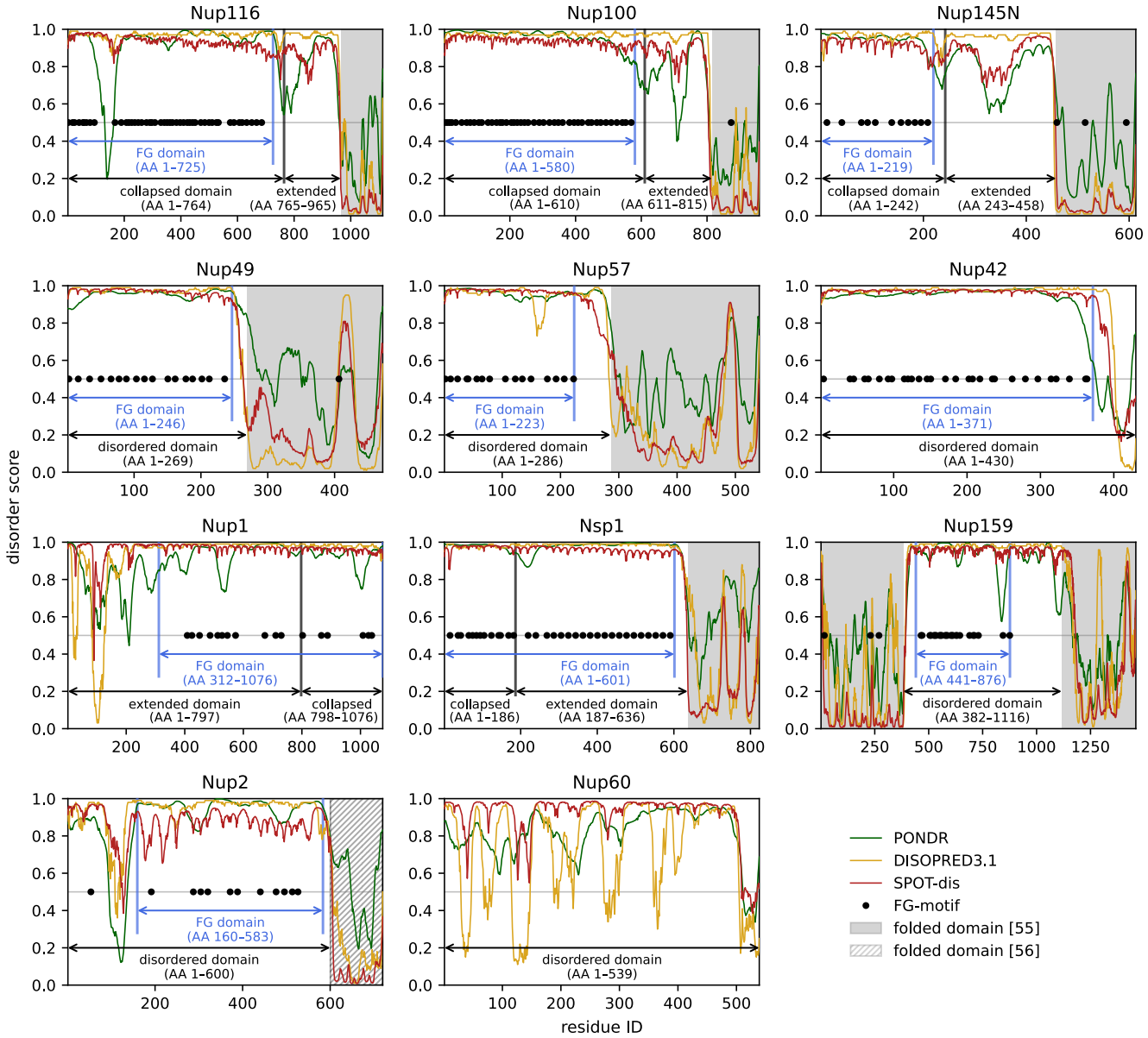

Fig. 1. Selection of FG-Nup domains based on the intrinsic disorder and location of FG motifs. Disorder prediction scores for the full-length FG-Nups are obtained from three different disorder predictors: PONDR (57), DISOPRED (58) and SPOT-Disorder (59). Horizontal gray lines mark the boundary between disordered (scores > 0.5) and not disordered (scores < 0.5). Shaded areas indicate folded domains as previously identified by Kim et al. (55) and are in excellent agreement with the disorder prediction scores. Black dots mark the position of the FG motifs in the sequence. The selected FG domains that are used in our simulations are marked by blue arrows and the disordered domains by black arrows. For the FG-Nups with a bimodal charge distribution [i.e., Nup116, Nup100, Nup145N, Nup1, and Nsp1 (10)], the collapsed and extended sections of the full disordered domain are indicated explicitly.

(*SI Appendix*, Fig. S5), forming a condensate with a slightly higher dense concentration (ρ_H = 385 ± 13 mg/mL) than Nup49. Interestingly, the dilute concentration (ρ_L = 0.13 ± 0.12 mg/mL) is significantly lower than that of Nup49 and actually comparable to that of the longer GLFG-Nups Nup116 and Nup100. Considering that Nup49x2 has the exact same charge-to-hydrophobicity ratio and the same density of FG motifs, this shows that also the protein length is important for the phase behavior of FG-Nups.

None of the FxFG-Nups phase separate at or below a concentration of 8 mg/mL. This does, however, not guarantee that these FG-Nups will not undergo phase separation at higher concentrations. To get a broader understanding of the phase behavior of the FG-Nups, we determined the full phase diagrams for each FG domain (*SI Appendix*, Fig. S7). We applied the Gaussian Cluster Theory (GCT) from Raos and Allegra (61, 62) adapted for protein systems by Zeng et al. (63) to compute the two- and three-body interaction coefficients from single-chain simulations (see *SI Appendix*, section 2 for more details). The phase diagrams of the GLFG-Nups are very similar and display critical temperatures for phase separation in the range of 340 to 380 K, meaning that we are well in the phase separation regime at 300 K, in agreement with our results (Fig. 2). Furthermore, for the FxFG-Nups that did not phase separate in our simulations, the critical temperature for phase separation is well below 300 K, confirming that these FG-Nups will not phase separate at 300 K. Given that the critical temperature for the FG-Nups without phase separation is significantly below the simulated temperature, we also conclude that our observations are not limited by the finite size of our simulations.

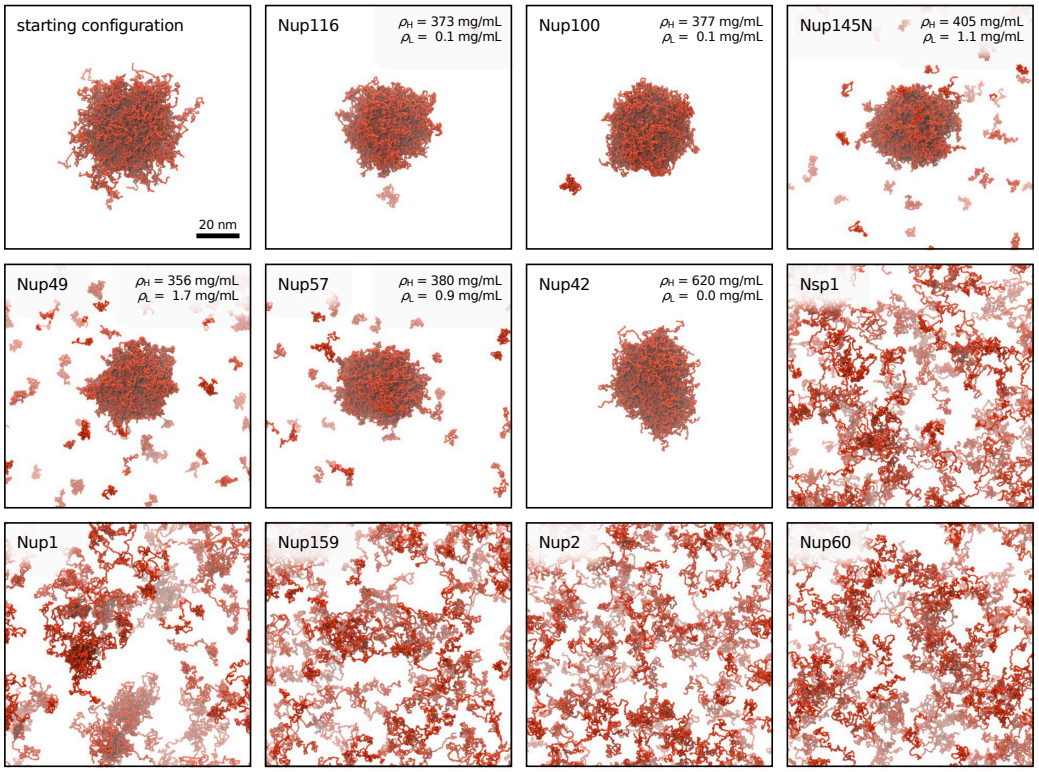

Fig. 2. Overview of the phase separation behavior of each FG-Nup. An example of a starting configuration (Nup49) that is used for each simulation is shown next to simulation snapshots of each FG-Nup system at $t^* = 5$ μs. Phase separation is observed for the FG domains of Nup116, Nup100, Nup145N, Nup49, Nup57, and Nup42. For the systems where a stable condensate exists, the concentrations of the dense phase and dilute phase, ρ_H and ρ_L, determined from radial density distributions (*SI Appendix*, Fig. S4) are shown in the top right corner of each snapshot.

In *SI Appendix*, Table S4, we compare the observed phase separation behavior in our simulations to experimental results. The observed phase separation behavior for each of the FG-Nups is in good qualitative agreement with the experimental studies. The FG domain of Nsp1 (AA 1–601) does not phase separate in our simulations, whereas some in vitro experiments have shown Nsp1 to form hydrogels (7, 26, 31, 37). These hydrogels are suggested to be stabilized by cross-β interactions (31), which are not explicitly accounted for in the 1BPA model. Nevertheless, we also note that other experiments did not observe phase separation of the FG domain of Nsp1 either (10, 38), in line with our findings.

In order to assess which residues are driving the phase separation of FG-Nups, we analyzed the intermolecular contact statistics in each of the FG-Nup condensates. We first determined the time-averaged number of intermolecular contacts per protein replica as a function of the residue number (see the "heat maps" of high and low interacting regions along the sequences of each FG-Nup in *SI Appendix*, Figs. S8 and S9). Because the different FG-Nups drastically vary in length, the absolute contact numbers are not directly comparable between FG-Nup systems, yet they do highlight the most important interacting regions of each sequence. To be able to quantitatively compare the intermolecular contacts independently of the protein chain length, we summed the contacts over all contact pairs for each residue (Fig. 3*A*). These one-dimensional contact summations display the number of interresidue contacts made by each individual residue. Upon marking the location of the FG motifs (dashed lines in Fig. 3*A*), we observe that many of the high contact peaks along the chains perfectly align with the location of FG motifs. This shows that most of the intermolecular contacts in the FG-Nup condensates are with FG motifs and that the high-intensity spots in the full contact maps represent FG–FG interactions. These high contact probabilities for FG motifs are observed in intramolecular contact maps of single-chain simulations as well, even in the case of FG-Nups that do not phase separate (*SI Appendix*, Fig. S12). This suggests that the presence of FG motifs alone is not enough for FG-Nups to undergo phase separation, but that also the cohesiveness of the spacers plays an important role.

To further investigate the interactions that are stabilizing FG-Nup condensates, we next analyzed the time-averaged number of intermolecular contacts per protein replica as a function of residue type (Fig. 3*B*). The contact maps are normalized for amino acid abundance. We find that the contact maps for each of the GLFG-Nups are highly similar with most intermolecular interactions involving F and L residues. This highlights the importance of both residues for FG-Nup phase separation. This observation is supported by recent mutation studies that showed that mutating either F or L of GLFG motifs into A results in a loss of phase separation (30).

Our observations highlight the "stickers and spacers" (60, 64) architecture of FG-Nups. Here, the FG motifs are the stickers that form FG–FG cross-links and thereby induce the formation of droplet-spanning percolated networks (20, 65, 66), while the FG-spacers modulate the interplay between chain–chain and chain–solvent interactions (66) and actually are the main determining factor for phase separation in FG-Nup systems. In each of the FG-Nup condensates, around 50% of the FG motifs is involved in FG–FG interactions (*SI Appendix*, Fig. S13). Surprisingly, these FG–FG interactions are highly dynamic, with FG–FG contacts existing for only ∼ 1 ps in our simulations

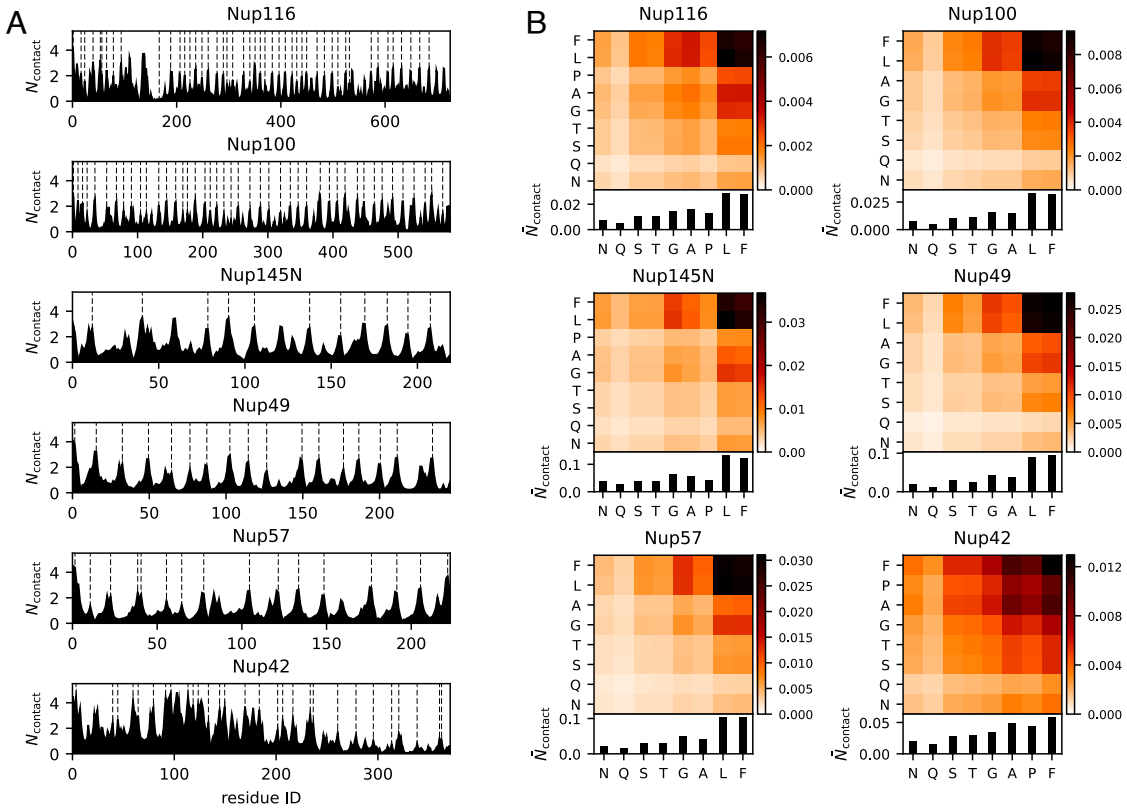

Fig. 3. Characterizing intermolecular interactions in FG-Nup condensates. (*A*) Time-averaged number of intermolecular contacts per protein replica in the condensed phases of Nup116, Nup100, Nup145N, Nup49, Nup57, and Nup42 as a function of the residue number. The dashed lines indicate the location of FG motifs. Full contact maps showing the intermolecular contacts per residue pair are shown in *SI Appendix*, Figs. S8 and S9. (*B*) Time-averaged number of intermolecular contacts per protein replica in the condensed phases of Nup116, Nup100, Nup145N, Nup49, Nup57, and Nup42 as a function of residue type. The contact maps are normalized for residue abundance, and only residues that contribute at least 4% to the amino acid sequence are shown. The *Top* panels show the (normalized) number of contacts between any pair of residue type; the *Bottom* panels show the total contact numbers per residue type. The non-normalized contact maps can be found in *SI Appendix*, Figs. S8 and S9.

(*SI Appendix*, Fig. S14). After correcting for the coarse-grained dynamics speed-up (*SI Appendix*, section 1.2), we find that the actual lifetime of FG–FG contacts is ∼ 0.5 ns. The contact lifetime of other interresidue contacts such as S–S or A–A is even shorter than that of FG–FG contacts. These short interaction lifetimes highlight the highly dynamic nature of the percolated networks present in the FG-Nup condensates, giving the droplets a liquid-like character as also corroborated by the continuous exchange of molecules between the dense and dilute phases.

Phase Separation of Bimodal FG-Nups. In the simulations above, we have used the FG domain of the FG-Nups (blue domains in Fig. 1). However, several FG-Nups display a bimodal distribution of charged amino acids in their disordered domains, resulting in a collapsed and an extended domain (10), which are also indicated in Fig. 1. Because of the ascribed importance of the bimodal character of the FG-Nups to the selectivity of the NPC's permeability barrier (10), we also investigated the role of bimodal charge distribution on the phase behavior of the different FG-Nups.

First of all, three of the central channel GLFG-Nups (Nup116, Nup100, and Nup145N) exhibit a clear bimodal charge distribution in their amino acid sequence (10). Since the extended (stalk) domains of these FG-Nups are lacking FG motifs, these domains were not included in the FG domains used above (Figs. 2 and 3). However, in view of their significant length (∼200 residues), it is reasonable to assume that these stalk domains impact the phase behavior of these FG-Nups. We have therefore repeated the phase separation simulations of Nup116, Nup100, and Nup145N, now including the extended stalk domains (hereafter named Nup116+, Nup100+, and Nup145N+, respectively). When setting up these simulations in a similar manner as for the FG domains, we noticed that the repulsive extended domains break up the initial condensate structure, forming smaller micelle-like condensates with the noncohesive extended domains residing on the surface of the condensates. Subsequently, these condensates started to coalesce, forming larger condensates. To avoid simulating this process, we built our initial condensate structure closer to the expected equilibrium state: a condensate structure with the cohesive collapsed domains in the center and the noncohesive extended domains at the outside.

Starting from this modified structure, we have simulated the FG-Nup systems for at least 5 μs and observed that again the equilibrium state is reached within 2 μs (*SI Appendix*, Fig. S3). Phase separation is now only observed for Nup116+ and Nup100+, where both FG-Nup condensates show similar conformations as the initial micelle-like structure (Fig. 4*A*). In both simulations, we observed a dynamic equilibrium state with a continuous exchange of molecules between the condensate and the dilute phase, showing that the initial conformation is not biasing the observed equilibrium state. We note that the dilute concentrations for both Nup116+ and Nup100+ are slightly higher than for the respective FG domain condensates. On the other hand, the densities of the Nup116+ and Nup100+ condensates are slightly lower than the FG domain case (Fig. 4*A* and *SI Appendix*, Fig. S4).

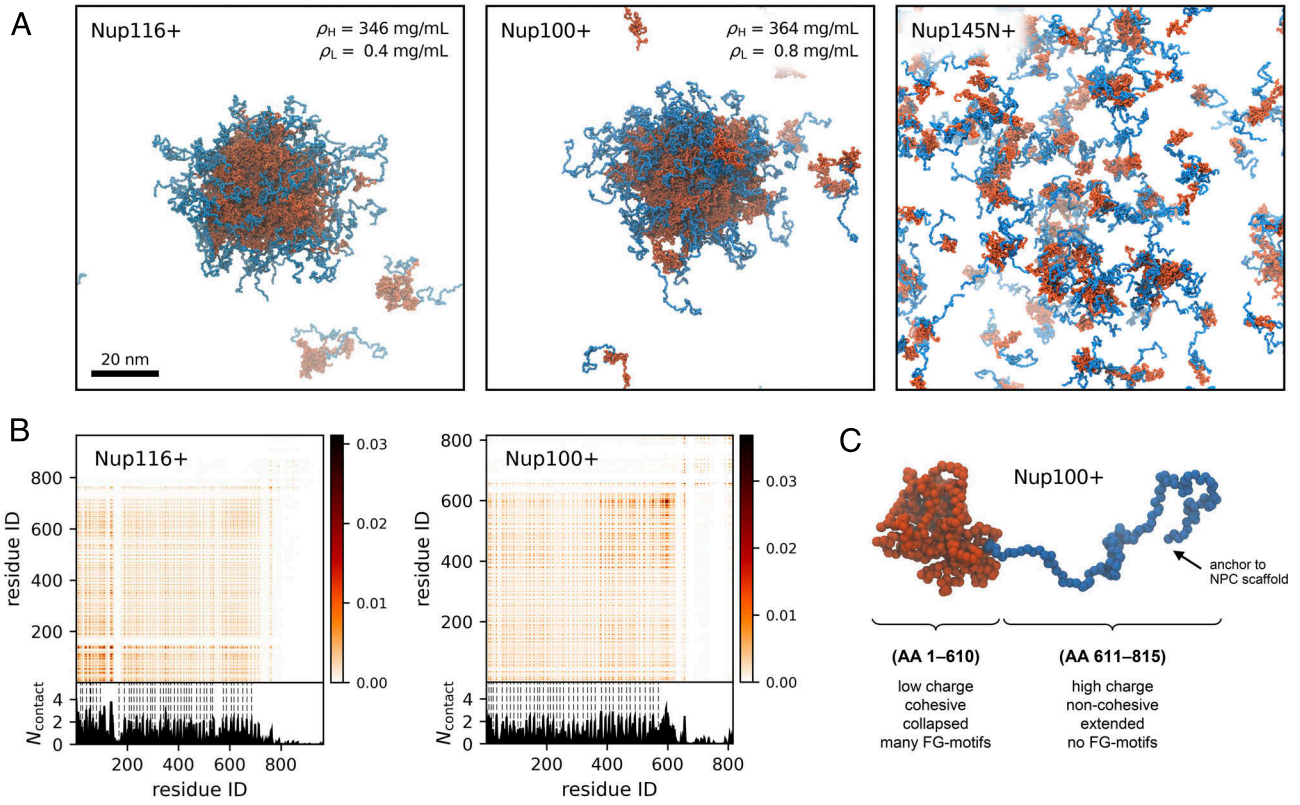

Fig. 4. Phase separation of the bimodal Nup116+, Nup100+, and Nup145N+. (*A*) Snapshots of the equilibrium states at $t^* = 5$ μs. Phase separation is observed for Nup116+ and Nup100+, where both condensates display a micelle-like structure: Cohesive FG domains (red) form the core of the condensate with the extended stalk domains (blue) on the outside. Separation of phases is not observed for Nup145N+. For Nup116+ and Nup100+, the concentrations of the dense phase and dilute phase, ρ_H and ρ_L, determined from radial density distributions (*SI Appendix*, Fig. S4) are shown in the top right corner of the snapshots. (*B*) Time-averaged number of intermolecular contacts per protein replica in the condensed phases of Nup116+ and Nup100+ as a function of residue number. The bottom figures show the one-dimensional summation, where the dashed lines indicate the location of the FG motifs. The contact analysis per residue type of Nup116+ and Nup100+ can be found in *SI Appendix*, Fig. S10. (*C*) The bimodal character of Nup100+. The cohesive collapsed domain (red) contains many FG motifs; the noncohesive extended domain (blue) is devoid of any FG motifs.

The intermolecular contact maps for the Nup116+ and Nup100+ condensates (Fig. 4*B*) confirm that the extended domains have only little interaction with the collapsed domains. Moreover, we note that the intermolecular contacts of the collapsed domain are very similar to those in the FG domain condensates (*SI Appendix*, Fig. S8). Nup145N+ did not display a separation of phases (Fig. 4*A*), which might be caused by two factors: First of all, we note that the FG domain of Nup145N has a lower phase separation propensity than the FG domains of Nup116 and Nup100, suggested by the higher concentration of the dilute phase (the saturation concentration) of Nup145N. In addition, the cohesive domain of Nup145N is significantly shorter than the cohesive domain of Nup116 and Nup100, while the lengths of the stalk domains are comparable for all three FG-Nups. Clearly, the difference in length ratios of the collapsed and extended domains plays an important role in phase separation, which warrants further investigation.

The Collapsed Domains of Nsp1 and Nup1 Do Phase Separate. Besides Nup116, Nup100, and Nup145N as discussed in the previous section, Nsp1 and Nup1 also feature a bimodal charge distribution in their sequence (Fig. 1). Rather than a collapsed domain with FG motifs and an extended domain devoid of FG motifs, the bimodality for Nsp1 and Nup1 is within their FG domain. In the foregoing simulations, we observed no phase separation for the FG domains of Nsp1 and Nup1. Although Nup1 did not form a large condensate as was observed for the GLFG-Nups and Nup42, the phase separation simulation of Nup1 did show small clusters (5 to 10 molecules, Fig. 2), which seem to be driven by the low-charge collapsed domains. To clarify the role of these domains, we also conduct phase separation simulations for the collapsed domains of Nsp1 and Nup1.

We find that the collapsed domains of Nsp1 and Nup1 both form stable condensates (Fig. 5*A*). Despite the fact that the collapsed domain of Nsp1 mostly contains regular FG motifs, its phase separation behavior is very similar to that of the GLFG-Nups, with concentrations of the dense phase and dilute phase that are comparable to those of GLFG-Nups. Intermolecular contact analysis highlights the considerable amount of FG interactions present in the Nsp1 condensate (Fig. 5*B* and *SI Appendix*, Fig. S11), driving the phase separation of this FG-Nup segment.

The collapsed domain of Nup1 contains only six FG motifs, yet it phase separates into a stable condensate. Intermolecular contact analysis again confirms the presence of FG interactions but also reveals that other F residues (not part of an FG motif) are involved in many of the intermolecular contacts (see Fig. 5*B*, red dashed lines). This highlights that, apart from FG motifs, a significant amount of hydrophobic residues can also induce phase separation of FG-Nups, in line with the findings in ref. 30. The dense concentration of the Nup1 condensate is significantly higher than the dense concentration of the GLFG-Nup condensates (*SI Appendix*, Fig. S4). This high concentration of the dense phase demonstrates the significant

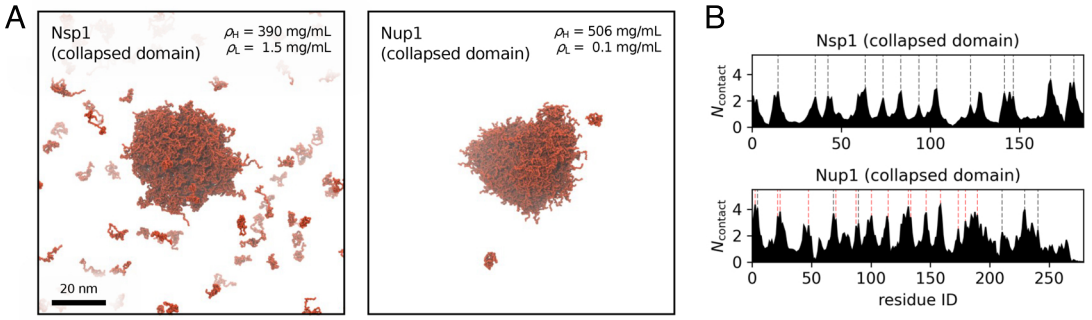

Fig. 5. Phase separation of the collapsed domains of Nsp1 and Nup1. (*A*) Snapshots of the equilibrium states at $t^* = 5$ μs. The concentrations of the dense phase and dilute phase, ρ_H and ρ_L, determined from radial density distributions (*SI Appendix*, Fig. S4) are shown in the top right corner of both snapshots. (*B*) Time-averaged number of intermolecular contacts per protein replica in the condensed phases of Nsp1 and Nup1 as a function of residue number. The black dashed lines indicate the location of FG motifs. For Nup1, the location of F residues is indicated by red dashed lines. Full contact maps showing the intermolecular contacts per residue pair are shown in *SI Appendix*, Fig. S11.

cohesiveness of the collapsed domain of Nup1, thus providing a possible explanation for the local FG-Nup clusters that we observed in the Nup1 FG domain simulation (Fig. 2).

Multiphase Organization of FG-Nups in an NPC Condensate. In the previous sections, we have characterized the phase behavior of homotypic FG-Nup systems. Next, we will analyze phase separation for a mixed FG-Nup system to study how the presence of different types of FG-Nups (with different phase separation propensities) can modulate the collective phase behavior. The composition of the FG-Nup mixture is identical to the stoichiometry of the yeast NPC (55), including the full disordered domain of each FG-Nup (Fig. 1). By doing so, we test the latent phase state of the disordered domain of the NPC by releasing the FG-Nups from their anchor points on the NPC scaffold.

For the initial configuration of this NPC condensate simulation, we have built an FG-Nup condensate consisting of all FG-Nups that phase separated in the homotypic simulations (GLFG-Nups and Nup42, see Fig. 2). FG-Nups that did not phase separate in the homotypic simulations (FxFG-Nups and Nup159, see Fig. 2) are not expected to phase separate in the NPC condensate simulation and are randomly placed in the dilute phase of the initial configuration (*SI Appendix*, Fig. S15). As a consequence of starting closer to the expected stable state, the dynamic equilibrium is reached significantly faster than when starting from an initial condensate structure containing all FG-Nups (see *Materials and Methods* for more details).

We have simulated the NPC condensate system for 10 μs, where a dynamic equilibrium is reached within 3 μs of simulation time (*SI Appendix*, Fig. S16). We observe a stable multiphase condensate accommodating the GLFG-Nups and Nup42 in different fractions (Fig. 6*A*). The NPC condensate has an average diameter of approximately 35 nm, which is smaller than the inner diameter of the scaffold structure of the yeast NPC (55, 67, 68). Similar to the homotypic phase separation

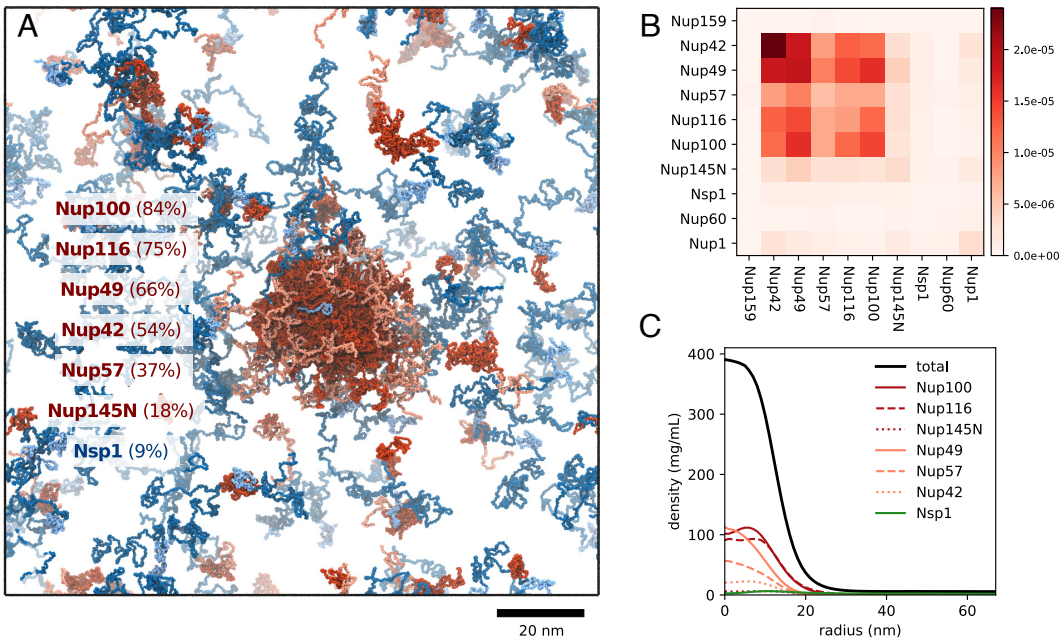

Fig. 6. Analysis of the NPC condensate. (*A*) Snapshot of the equilibrium state of the NPC condensate at $t^* = 10$ μs. The GLFG-Nups and Nup42 are colored in red, with the extended domains of Nup116, Nup100, and Nup145N colored in light red. FxFG-Nups and Nup159 are colored in blue, with the collapsed domains of Nsp1 and Nup1 colored in light blue. The FG-Nups making up the NPC condensate are reported inside the snapshot, along with the fraction of each FG-Nup that is found in the dense phase, averaged over the last 5 μs of the simulation (*SI Appendix*, Fig. S16). (*B*) Time-averaged number of intermolecular contacts per protein replica for all FG-Nup combinations. The contact numbers are normalized for FG-Nup abundance in the system. (*C*) Radial density distribution of the NPC condensate for the whole system and the most abundant FG-Nups in the dense phase.

simulations of Nup100+ and Nup116+, we again see that the noncohesive extended domains of Nup100, Nup116, and Nup145N (colored in light red in Fig. 6*A*) mostly reside on the periphery of the condensate.

The overall phase behavior of the different FG-Nups in the NPC condensate simulation is very similar to the homotypic phase separation simulations. However, there is a large variation in the phase separation propensity of the different FG-Nup types, which we observe from the different fractions of each FG-Nup present in the condensed phase. Most of the Nup100, Nup116, and Nup49 molecules are found in the condensed phase (70 to 90%), while only half of the Nup57 and Nup42 molecules are in the NPC condensate (40 to 50%). Surprisingly, whereas the full disordered domain of Nup145N did not phase separate in the homotypic case, here, a notable fraction of Nup145N (20%) is present in the condensed phase, showing that the phase separation propensity of FG-Nups can be modulated by the presence of other (phase-separating) FG-Nups.

From the homotypic phase separation simulations, we found that the FG domains of Nsp1 and Nup1 do not phase separate, while their collapsed domains do. In the NPC condensate, we observe a significant amount of intermolecular contacts of the collapsed domains of Nsp1 and Nup1 with the FG-Nup condensate, although Nsp1 and Nup1 are not able to phase separate into the dense phase.

Intermolecular contact analysis on the NPC condensate (Fig. 6*B*) reveals that there are interactions between each of the different FG-Nups in the NPC condensate. Most interactions are between the GLFG-Nups and Nup42, which is not surprising considering their high abundance in the NPC condensate. The extensive amount of contacts with Nup42 is somewhat remarkable, as only 50% of the Nup42 monomers are in the condensed phase. This underlines the strong cohesive interactions of Nup42, as was seen before in the high density of the Nup42-condensate. The full contact map, including intermolecular contacts per residue index (*SI Appendix*, Fig. S17), reveals that the heterotypic interactions between FG-Nups are between the same domains as the homotypic interactions. In particular, we see that the extended domains of Nup100, Nup116, and Nup145N are almost completely devoid of any intermolecular interactions. On the other hand, a significant amount of contacts is observed for the collapsed domain of Nup1 (mostly with Nup42 and Nup145N present in the dilute phase).

Discussion

In this work, we used coarse-grained MD simulations at amino acid resolution to study the phase separation of intrinsically disordered FG-Nups with the aim to identify the main physicochemical driving forces for the formation of FG-Nup condensates. We tested the phase separation behavior over the full range of yeast FG-Nups and found that the FG domains of the GLFG-Nups and Nup42 phase separate into stable liquid-like condensates that are in dynamic equilibrium with the surrounding solvent. No phase separation is observed for the FG domains of any of the FxFG-Nups and Nup159. Our results are in good qualitative agreement with experiments for both the phase-separating and nonphase-separating FG-Nups (*SI Appendix*, Table S4). Full phase diagrams obtained using Gaussian cluster theory from single-chain simulations (*SI Appendix*, Fig. S7) show that our observations are not biased by the used protein concentration or the limited number of proteins in the simulations.

The difference in phase separation behavior between the GLFG and FxFG-Nups is striking. The reason for this is twofold. First of all, the FG motif density is generally lower in FxFG-Nups than in GLFG-Nups (*SI Appendix*, Table S5). Second, the charge-to-hydrophobicity ratio (C/H) of the FG-spacers is higher for FxFG-Nups than for GLFG-Nups (*SI Appendix*, Table S5). From this, the following picture emerges: Phase separation of FG-Nups is driven by hydrophobic FG motifs that act as stickers, whose ability to actually form FG–FG cross-links is mediated by the cohesiveness of the FG-spacers. We note that the cationic and anionic residues in FG-Nups are homogeneously distributed along the sequences, resulting in a very low net charge along each of the FG domains, so that electrostatic interactions do not play a big role. Nevertheless, because of their polar character, the charged amino acids have a significant impact on the cohesiveness of the FG-spacers.

Recent experiments have shown that some FG-Nups undergo phase separation with a lower critical solution temperature (30), i.e., phase separation is enhanced by increasing the temperature. Such temperature dependence is not present in our simulations as the molecular interactions in our CG model are calibrated at a specific temperature. Indeed, the calculated phase diagrams show that in our simulations, all FG-Nups undergo phase separation with an upper critical temperature.

Intermolecular contact analysis of the obtained FG-Nup condensates revealed the highly dynamic FG–FG interactions as the main interactions stabilizing FG-Nup condensates. This is consistent with mutation studies that showed that mutating the F of the FG motifs into A results in loss of phase separation (30, 38). A closer look at the residues that are involved in the intermolecular interactions reveals the general importance of hydrophobic residues for phase separation of FG-Nups. Besides the high contact numbers for F residues, we also find a similar amount of interactions with L residues (mostly part of GLFG motifs), suggesting equal importance of both F and L residues in the GLFG motifs. This is supported by recent observations that mutating either the F or L of GLFG motifs into A (less hydrophobic) results in the absence of phase separation (30). It should also be noted that recent experiments have shown that interactions between aromatic residues (such as F–F interactions) are stronger than regular hydrophobic interactions (such as L–L or L–F interactions) (64). Aromatic residues in our model, however, merely interact through nonspecific hydrophobic interactions; specific π–π stacking or T-stacking interactions that might be present between the FG motifs (7, 30) are not included.

Besides the FG domains of each of the FG-Nups, we have also studied several other FG-Nup segments, specifically in the case of FG-Nups that have a bimodal charge distribution along their sequences. First of all, we have looked at the full disordered domains of Nup116, Nup100, and Nup145N. Apart from a cohesive FG domain, these FG-Nups also have an extended domain containing a large fraction of charged residues and no FG motifs. Upon inclusion of these extended domains into the FG-Nup sequences, Nup100+ and Nup116+ still phase separated. The noncohesive extended domains largely reside on the periphery of the condensates, forming micelle-like structures, and do not significantly participate in intermolecular interactions. This relative positioning is similar in the NPC, where these extended domains connect the FG domains to the NPC scaffold (55, 56). These noncohesive domains then form areas of low protein density between the NPC scaffold and the

central cohesive FG-meshwork, in correspondence with previous modeling results (40) and the forest model (10).

Finally, we studied the intermolecular interactions in a multiphase FG-Nup condensate with a stoichiometry equal to the yeast NPC. Here, we observed a GLFG-condensate, composed of all the GLFG-Nups and Nup42, that is again stabilized by dynamic FG–FG interactions. These are the same FG-Nups for which homotypic phase separation was observed, and the same interactions are responsible for the phase separation of the NPC condensate. The dilute (saturation) concentration of the NPC condensate is surprisingly high, with much higher fractions of free GLFG-Nups compared to the homotypic GLFG-Nup condensates.

Although enticing, our results do not indicate that the FG-meshwork in the core of the NPC is a biomolecular condensate. Directly relating FG-Nup phase separation to the phase state of the NPC's selective permeability barrier is misplaced, simply because the FG-Nups in the NPC are tethered to the scaffold and thus cannot display the characteristic properties associated with phase separation (e.g., surface tension, self-diffusion, dynamic exchange). Nevertheless, we note that most of the FG-Nups for which we observed phase separation (in the untethered state) are located at the center of the yeast NPC (Nup116, Nup100, Nup145N, Nup49, and Nup57), while FG-Nups that do not phase separate are located at the cytoplasmic and nucleoplasmic sides of the NPC (Nup159, Nup1, Nup2, and Nup60). This suggests that the phase separation propensity of FG-Nups is related to the location and function in the NPC and the following picture of the organization of the FG-Nups inside the NPC emerges: The central channel (mostly GLFG) Nups form a dense, highly dynamic percolated network constituting many FG–FG interactions, while the peripheral (mostly FxFG) Nups form an entropic brush at the cytoplasmic and nucleoplasmic sides.

Materials and Methods

Coarse-Grained Model for Disordered Proteins. All coarse-grained MD simulations are done with the 1BPA-1.1 model for intrinsically disordered proteins. This implicit-solvent model at amino acid resolution displays realistic backbone conformations and accounts for hydrophobic, electrostatic, and cation–π interactions (39–41, 53). Several hydrophobic interactions are fine-tuned to better match the experimental Stokes radii of yeast FG-Nup segments (see *SI Appendix*, section 1 for a detailed description). All simulations are performed at 300 K and physiological salt concentration of 150 mM using GROMACS (69) molecular dynamics software (version 2019.4), where the stochastic dynamics integrator operates with a time step of 0.02 ps and inverse friction coefficient γ^{-1} = 50 ps. More details on the model and the coarse-grained dynamics speed-up factor are provided in *SI Appendix*.

FG-Nup Phase Separation Simulations. To set up the system, we created a condensate structure by performing an NVT equilibration in a cubic periodic box at a density of 2 beads per nm^3 (~350 mg/mL), which is comparable to the densities of FG-Nup condensates (28, 60). The initial state of this NVT simulation is generated by dividing the simulation volume into equal cubes ($N_{\text{cubes}} \geq N_{\text{monomers}}$) and tightly packing each monomer inside one of these cubes in a zigzag-like pattern (*SI Appendix*, Fig. S2). The high-density NVT simulation is run for 500 ns to mix the monomer solution. Then, the periodic box dimensions are increased by 350% with the protein condensate at the center (see Fig. 2 for an example of the initial configuration), resulting in an overall concentration of approximately 8 mg/mL. This approach significantly speeds up the convergence to a dynamic equilibrium state compared to starting from a homogeneous monomer solution. For each FG-Nup system, a system size was chosen such that the total number of amino acids is close to 70,000 beads, which is sufficiently large so that finite size effects in the simulations are small. The FG-Nup systems are simulated for 5 μs, where dynamic equilibrium is typically reached within the first 2 μs (*SI Appendix*, Fig. S3). We also performed an additional simulation for Nup49 (*SI Appendix*, Fig. S3), where we started with 50% of the molecules in the dilute phase instead, confirming that the obtained equilibria are independent of the chosen starting configuration.

Cluster sizes (*SI Appendix*, Fig. S3) are determined using the "gmx clustsize" utility of GROMACS, where two monomers are considered to be in the same cluster if at least two residues of those monomers are within 0.7 nm (53).

NPC Condensate Phase Separation Simulation. The phase separation simulation for the NPC condensate could be set up in a similar way as the homotypic FG-Nup phase separation simulations (i.e., starting from a condensate structure containing all FG-Nups). However, due to strong repulsive interactions from several noncohesive FG-Nup domains (e.g., Nup159, Nup60), the initial condensate structure quickly falls apart and cohesive FG-Nups phase separate again into smaller condensate structures. Given enough time, these smaller condensates will eventually merge into a single condensate again, but considering the large system size and the slow diffusion speed of the condensates, this takes tens of microseconds.

To prevent excessive repulsive interactions in the initial condensate structure, we have created an initial condensate structure containing only FG-Nups that are likely to phase separate: Nup116, Nup100, Nup145N, Nup49, Nup57, and Nup42 (cf. Fig. 2). The high-density condensate simulation is equilibrated for 500 ns (NVT), after which the box dimensions are increased and the noncohesive FG-Nups are randomly distributed around the FG-Nup condensate, where the protein backbone conformations are sampled from single-chain simulations. The final box dimensions are chosen such that the concentration is the same as in the homotypic phase separation simulations. The resulting structure is a condensate containing all cohesive FG-Nups, surrounded by a dilute phase that contains a homogeneous solution of noncohesive FG-Nups (*SI Appendix*, Fig. S15). This initial configuration is then simulated for 10 μs, where the last 5 μs are used for analysis of the NPC condensate (*SI Appendix*, Fig. S16).

Radial Density Profiles. Radial density profiles are obtained by determining the average density in discrete concentric shells of thickness 1 nm measured from the center of the condensate. The radial density profiles (Fig. 6*C* and *SI Appendix*, Fig. S4) are time-averaged over the last 3 μs of the simulation, where a density profile is determined every nanosecond. The concentration of the dense phase is obtained from the radial density profiles by averaging the density from $r = 0$ up to the boundary of the high-density region (chosen at the r value, where $|d\rho/dr| = 4$ mg/mL/nm, see the left dashed lines in *SI Appendix*, Fig. S4). Similarly, the dilute concentrations, ρ_L, are obtained by averaging the density starting from the boundary of the low-density region (chosen at the r value where $|d\rho/dr| = 0.1$ mg/mL/nm, see the right dashed lines in *SI Appendix*, Fig. S4) until $r = 55$ nm.

Intramolecular Contact Analysis. The intramolecular contact analyses (*SI Appendix*, Fig. S12) are performed on single-chain simulations. For each trajectory frame (sampled every 0.2 ns over a 10-μs long trajectory), an upper triangular contact matrix is computed that describes all interresidue contacts within the protein chain. Here, any residue pair is considered to form a contact when the distance separating the beads is less than 0.7 nm. We considered only the intramolecular contacts between beads that are at least three residues apart in the sequence. The average contact map is then calculated by averaging over all trajectory frames.

Intermolecular Contact Analysis of the Homotypic FG-Nup Condensates. For the intermolecular contact analyses of the homotypic FG-Nup condensates (Figs. 3, 4*B*, and 5*B* and *SI Appendix*, Figs. S8–S11), we considered only the interactions between FG-Nups inside the condensates. For each trajectory frame (sampled every 1 ns over the final 3 μs of the trajectory), we first determined which molecules are part of the condensate using the "gmx clustsize" utility of GROMACS. Here, a protein chain is considered to be part of the condensate if at least one of the residues is within 0.7 nm of any bead of the condensate. Then, for each unique pair of chains in the condensate, a contact matrix is computed, resulting in $N_{\text{Nup}}(N_{\text{Nup}} - 1)/2$ contact matrices (where N_{Nup} is the number of FG-Nup proteins in the condensate). The average number of intermolecular contacts is then obtained by summing all the individual contact matrices and

Table 1. Composition of the NPC condensate simulation, where the number of each FG-Nup is the same as in the yeast NPC (55). For each FG-Nup, the full disordered domain is used (Fig. 1). The FG-Nups are placed either in the dense phase or dilute phase of the initial configuration based on their expected phase behavior; see Fig. 2

FG-Nup	Domain	Frequency	Cohesive
Nup116	AA 1–965	16	Yes
Nup100	AA 1–815	16	Yes
Nup145N	AA 1–458	16	Yes
Nup49	AA 1–269	32	Yes
Nup57	AA 1–286	32	Yes
Nup42	AA 1–430	8	Yes
Nup1	AA 1–1076	8	No
Nsp1	AA 1–636	48	No
Nup159	AA 382–1116	16	No
Nup60	AA 1–539	16	No

normalizing for the number of chains in the condensate. Finally, these contact maps are averaged over the trajectory.

Intermolecular Contact Analysis of the NPC Condensate. For the intermolecular contact analysis of the NPC condensate (Fig. 6*B* and *SI Appendix*, Fig. S17), no distinction is made between FG-Nups that are in the condensate or in the dilute phase. For each trajectory frame (sampled every 1 ns over the final 5 μs of the trajectory), the full contact matrix is computed for each unique pair of chains in the system. Because the different FG-Nups are present in different quantities (Table 1), we normalized the contact map for each FG-Nup pair by the product of the abundance of both FG-Nups. In the case of the homotypic contact maps, we did not consider the intramolecular contacts in the averaging process. Therefore, the normalization factor is here $N_i(N_i - 1)$ instead of N_i^2, where N_i is the number of chains of FG-Nup i in the system. This results in the contact map per residue index for each FG-Nup type (lower triangle of *SI Appendix*, Fig. S17).

To obtain the relative contact frequency between different types of FG-Nups (Fig. 6*B* and the upper triangle of *SI Appendix*, Fig. S17), we averaged the normalized contact numbers per index. Because the FG-Nups have different chain lengths, we also normalized the contact number for each FG-Nup pair by the product of the chain length of both FG-Nups.

Data, Materials, and Software Availability. All study data are included in the article and/or *SI Appendix*.

ACKNOWLEDGMENTS. This work was financially supported by the Netherlands Organization of Scientific Research grant no. OCENW.GROOT.2019.068. This work made use of the Dutch national e-infrastructure with the support of the SURF Cooperative using grant no. EINF-3473. We thank the Center for Information Technology of the University of Groningen for their support and for providing access to the Peregrine high-performance computing cluster.

1. M. P. Rout, J. D. Aitchison, The nuclear pore complex as a transport machine. *J. Biol. Chem.* **276**, 16593–16596 (2001).
2. L. J. Terry, S. R. Wente, Flexible gates: Dynamic topologies and functions for FG nucleoporins in nucleocytoplasmic transport. *Eukaryotic Cell* **8**, 1814–1827 (2009).
3. B. B. Hülsmann, A. A. Labokha, D. Görlich, The permeability of reconstituted nuclear pores provides direct evidence for the selective phase model. *Cell* **150**, 738–751 (2012).
4. C. Li, A. Goryaynov, W. Yang, The selective permeability barrier in the nuclear pore complex. *Nucleus* **7**, 430–446 (2016).
5. B. L. Timney *et al*., Simple rules for passive diffusion through the nuclear pore complex. *J. Cell Biol.* **215**, 57–76 (2016).
6. K. Ribbeck, D. Görlich, Kinetic analysis of translocation through nuclear pore complexes. *EMBO J.* **20**, 1320–1330 (2001).
7. S. Frey, R. P. Richter, D. Görlich, FG-rich repeats of nuclear pore proteins form a three-dimensional meshwork with hydrogel-like properties. *Science* **314**, 815–817 (2006).
8. M. P. Rout *et al*., The yeast nuclear pore complex: Composition, architecture, and transport mechanism. *J. Cell Biol.* **148**, 635–652 (2000).
9. R. Y. H. Lim *et al*., Flexible phenylalanine–glycine nucleoporins as entropic barriers to nucleocytoplasmic transport. *Proc. Natl. Acad. Sci. U.S.A.* **103**, 9512–9517 (2006).
10. J. Yamada *et al*., A bimodal distribution of two distinct categories of intrinsically disordered structures with separate functions in FG nucleoporins. *Mol. Cell. Proteom.* **9**, 2205–2224 (2010).
11. R. Y. Lim, B. Huang, L. E. Kapinos, How to operate a nuclear pore complex by Kap-centric control. *Nucleus* **6**, 366–372 (2015).
12. L. E. Kapinos, B. Huang, C. Rencurel, R. Y. H. Lim, Karyopherins regulate nuclear pore complex barrier and transport function. *J. Cell Biol.* **216**, 3609–3624 (2017).
13. C. P. Brangwynne, P. Tompa, R. V. Pappu, Polymer physics of intracellular phase transitions. *Nat. Phys.* **11**, 899–904 (2015).
14. S. Alberti, A. Gladfelter, T. Mittag, Considerations and challenges in studying liquid–liquid phase separation and biomolecular condensates. *Cell* **176**, 419–434 (2019).
15. S. Boeynaems *et al*., Protein phase separation: A new phase in cell biology. *Trends Cell Biol.* **28**, 420–435 (2018).
16. S. Xiang *et al*., The LC domain of hnRNPA2 adopts similar conformations in hydrogel polymers, liquid-like droplets, and nuclei. *Cell* **163**, 829–839 (2015).
17. D. Hnisz, K. Shrinivas, R. A. Young, A. K. Chakraborty, P. A. Sharp, A phase separation model for transcriptional control. *Cell* **169**, 13–23 (2017).
18. J. E. Henninger *et al*., RNA-mediated feedback control of transcriptional condensates. *Cell* **184**, 207–225.e24 (2021).
19. A. R. Tejedor, A. Garaizar, J. Ramírez, J. R. Espinosa, RNA modulation of transport properties and stability in phase-separated condensates. *Biophys. J.* **120**, 5169–5186 (2021).
20. M. Kar *et al*., Phase-separating RNA-binding proteins form heterogeneous distributions of clusters in subsaturated solutions. *Proc. Natl. Acad. Sci. U.S.A.* **119**, e2202222119 (2022).
21. M. Kato *et al*., Cell-free formation of RNA granules: Low complexity sequence domains form dynamic fibers within hydrogels. *Cell* **149**, 753–767 (2012).
22. J. Wang *et al*., A molecular grammar governing the driving forces for phase separation of prion-like RNA binding proteins. *Cell* **174**, 688–699.e16 (2018).
23. S. Qamar *et al*., FUS phase separation is modulated by a molecular chaperone and methylation of arginine cation–π interactions. *Cell* **173**, 720–734.e15 (2018).
24. G. H. Kim, I. Kwon, Distinct roles of hnRNPH1 low-complexity domains in splicing and transcription. *Proc. Natl. Acad. Sci. U.S.A.* **118**, e2109668118 (2021).
25. G. Celetti *et al*., The liquid state of FG-nucleoporins mimics permeability barrier properties of nuclear pore complexes. *J. Cell Biol.* **219**, e201907157 (2020).
26. S. Frey, D. Görlich, A saturated FG-repeat hydrogel can reproduce the permeability properties of nuclear pore complexes. *Cell* **130**, 512–523 (2007).
27. S. Frey, D. Görlich, FG/FxFG as well as GLFG repeats form a selective permeability barrier with self-healing properties. *EMBO J.* **28**, 2554–2567 (2009).
28. H. B. Schmidt, D. Görlich, Nup98 FG domains from diverse species spontaneously phase-separate into particles with nuclear pore-like permselectivity. *eLife* **4**, e04251 (2015).
29. S. C. Ng, T. Güttler, D. Görlich, Recapitulation of selective nuclear import and export with a perfectly repeated 12mer GLFG peptide. *Nat. Commun.* **12**, 4047 (2021).
30. E. E. Najbauer, S. C. Ng, C. Griesinger, D. Görlich, L. B. Andreas, Atomic resolution dynamics of cohesive interactions in phase-separated Nup98 FG domains. *Nat. Commun.* **13**, 1494 (2022).
31. C. Ader *et al*., Amyloid-like interactions within nucleoporin FG hydrogels. *Proc. Natl. Acad. Sci. U.S.A.* **107**, 6281–6285 (2010).
32. R. Halfmann, J. R. Wright, S. Alberti, S. Lindquist, M. Rexach, Prion formation by a yeast GLFG nucleoporin. *Prion* **6**, 391–399 (2012).
33. S. Milles *et al*., Facilitated aggregation of FG nucleoporins under molecular crowding conditions. *EMBO Rep.* **14**, 178–183 (2013).
34. E. F. E. Kuiper *et al*., The chaperone DNAJB6 surveils FG-nucleoporins and is required for interphase nuclear pore complex biogenesis. *Nat. Cell Biol.* **24**, 1584–1594 (2022).
35. A. Ibáñez de Opakua *et al*., Molecular interactions of FG nucleoporin repeats at high resolution. *Nat. Chem.* **14**, 1278–1285 (2022).
36. B. Hampoelz *et al*., Nuclear pores assemble from nucleoporin condensates during oogenesis. *Cell* **179**, 671–686.e17 (2019).
37. M. Petri, S. Frey, A. Menzel, D. Görlich, S. Techert, Structural characterization of nanoscale meshworks within a nucleoporin FG hydrogel. *Biomacromolecules* **13**, 1882–1889 (2012).
38. S. S. Patel, B. J. Belmont, J. M. Sante, M. F. Rexach, Natively unfolded nucleoporins gate protein diffusion across the nuclear pore complex. *Cell* **129**, 83–96 (2007).
39. A. Ghavami, E. Van der Giessen, P. R. Onck, Coarse-grained potentials for local interactions in unfolded proteins. *J. Chem. Theory Comput.* **9**, 432–440 (2013).
40. A. Ghavami, L. M. Veenhoff, E. Van der Giessen, P. R. Onck, Probing the disordered domain of the nuclear pore complex through coarse-grained molecular dynamics simulations. *Biophys. J.* **107**, 1393–1402 (2014).
41. H. Jafarinia, E. Van der Giessen, P. R. Onck, Molecular basis of C9orf72 poly-PR interference with the β-karyopherin family of nuclear transport receptors. *Sci. Rep.* **12**, 21324 (2022).
42. M. Peyro, M. Soheilypour, A. Ghavami, M. R. Mofrad, Nucleoporin's like charge regions are major regulators of FG coverage and dynamics inside the nuclear pore complex. *PLoS ONE* **10**, e0143745 (2015).
43. P. Popken, A. Ghavami, P. R. Onck, B. Poolman, L. M. Veenhoff, Size-dependent leak of soluble and membrane proteins through the yeast nuclear pore complex. *Mol. Biol. Cell* **26**, 1386–1394 (2015).
44. A. Ghavami, E. Van der Giessen, P. R. Onck, Energetics of transport through the nuclear pore complex. *PLoS ONE* **11**, e0148876 (2016).
45. A. Mishra, W. Sipma, L. M. Veenhoff, E. Van der Giessen, P. R. Onck, The effect of FG-Nup phosphorylation on NPC selectivity: A one-bead-per-amino-acid molecular dynamics study. *Int. J. Mol. Sci.* **20**, 596 (2019).
46. M. Peyro, A. M. Dickson, M. R. Mofrad, Nucleoporins' exclusive amino acid sequence features regulate their transient interaction with and selectivity of cargo complexes in the nuclear pore. *Mol. Biol. Cell* **32**, ar31 (2021).
47. D. Winogradoff, H. Y. Chou, C. Maffeo, A. Aksimentiev, Percolation transition prescribes protein size-specific barrier to passive transport through the nuclear pore complex. *Nat. Commun.* **13**, 5138 (2022).

48. A. N. Ananth *et al*., Spatial structure of disordered proteins dictates conductance and selectivity in nuclear pore complex mimics. *eLife* **7**, e31510 (2018).
49. P. Ketterer *et al*., DNA origami scaffold for studying intrinsically disordered proteins of the nuclear pore complex. *Nat. Commun.* **9**, 902 (2018).
50. A. Fragasso *et al*., A designer FG-Nup that reconstitutes the selective transport barrier of the nuclear pore complex. *Nat. Commun.* **12**, 2010 (2021).
51. A. Fragasso *et al*., Transport receptor occupancy in nuclear pore complex mimics. *Nano Res.* **15**, 9689–9703 (2022).
52. N. Klughammer *et al*., Diameter dependence of transport through nuclear pore complex mimics studied using optical nanopores. bioRxiv [Preprint] (2023). https://doi.org/10.1101/2023.02.18.529008 (Accessed 18 February 2023).
53. H. Jafarinia, E. Van der Giessen, P. R. Onck, Phase separation of toxic dipeptide repeat proteins related to C9orf72 ALS/FTD. *Biophys. J.* **119**, 843–851 (2020).
54. J. T. Nielsen, F. A. A. Mulder, Quality and bias of protein disorder predictors. *Sci. Rep.* **9**, 5137 (2019).
55. S. J. Kim *et al*., Integrative structure and functional anatomy of a nuclear pore complex. *Nature* **555**, 475–482 (2018).
56. D. P. Denning, M. F. Rexach, Rapid evolution exposes the boundaries of domain structure and function in natively unfolded FG nucleoporins. *Mol. Cell. Proteom.* **6**, 272–282 (2007).
57. S. Vucetic, C. J. Brown, A. K. Dunker, Z. Obradovic, Flavors of protein disorder. *Proteins* **52**, 573–584 (2003).
58. D. T. Jones, D. Cozzetto, DISOPRED3: Precise disordered region predictions with annotated protein-binding activity. *Bioinformatics* **31**, 857–863 (2015).
59. J. Hanson, Y. Yang, K. Paliwal, Y. Zhou, Improving protein disorder prediction by deep bidirectional long short-term memory recurrent neural networks. *Bioinformatics* **33**, 685–692 (2017).
60. S. C. Ng *et al*., Barrier properties of Nup98 FG phases ruled by FG motif identity and inter-FG spacer length. *Nat. Commun.* **14**, 747 (2023).
61. G. Raos, G. Allegra, Chain collapse and phase separation in poor-solvent polymer solutions: A unified molecular description. *J. Chem. Phys.* **104**, 1626–1645 (1996).
62. G. Raos, G. Allegra, Macromolecular clusters in poor-solvent polymer solutions. *J. Chem. Phys.* **107**, 6479–6490 (1997).
63. X. Zeng, A. S. Holehouse, A. Chilkoti, T. Mittag, R. V. Pappu, Connecting coil-to-globule transitions to full phase diagrams for intrinsically disordered proteins. *Biophys. J.* **119**, 402–418 (2020).
64. A. Bremer *et al*., Deciphering how naturally occurring sequence features impact the phase behaviours of disordered prion-like domains. *Nat. Chem.* **14**, 196–207 (2021).
65. T. S. Harmon, A. S. Holehouse, M. K. Rosen, R. V. Pappu, Intrinsically disordered linkers determine the interplay between phase separation and gelation in multivalent proteins. *eLife* **6**, e30294 (2017).
66. T. Mittag, R. V. Pappu, A conceptual framework for understanding phase separation and addressing open questions and challenges. *Mol. Cell* **82**, 2201–2214 (2022).
67. M. Allegretti *et al*., In-cell architecture of the nuclear pore and snapshots of its turnover. *Nature* **586**, 796–800 (2020).
68. C. W. Akey *et al*., Comprehensive structure and functional adaptations of the yeast nuclear pore complex. *Cell* **185**, 361–378.e25 (2022).
69. D. Van der Spoel *et al*., GROMACS: Fast, flexible, and free. *J. Comput. Chem.* **26**, 1701–1718 (2005).